Aerotecnica Missili & Spazio
https://doi.org/10.1007/s42496-023-00189-y

ORIGINAL ARTICLE

Experimental Validation of Virtual Wind Tunnel Testing for Ultra-low Reynolds Numbers Flows

Manuel Carreño Ruiz[1] · **Domenic D'Ambrosio**[1]

Received: 26 July 2023 / Revised: 20 October 2023 / Accepted: 30 October 2023

Abstract
The recent success of the Ingenuity Mars helicopter developed by the jet propulsion laboratory (JPL) demonstrated the feasibility of the Martian flight. Low pressure (660 Pa) and temperature (210 K) characterize the ground-level Martian atmosphere. Since such conditions are difficult and expensive to mimic on Earth, it is necessary to have reliable simulation tools that can correctly reproduce Martian aerodynamics. In the case of unmanned aerial systems (UAS), the latter is characterized by a high subsonic Mach number at the tip of the blades and an Ultra-low Reynolds number regime ($1000 < Re < 10000$). To this purpose, the laminar solver embedded in the commercial CFD code STAR CCM+ was validated by reproducing experiments carried out in the Martian Wind Tunnel at Tohoku University using a triangular airfoil wing at Reynolds 3000 and a Mach number of 0.5. Simulations are performed at angles of attack ranging from 0 to 16 degrees showing a satisfactory agreement with experimental results for very different flow conditions.

Keywords Ultra-low Reynolds numbers · Martian flight · Virtual testing · Computational fluid dynamics

1 Introduction

Flying in the Mars atmosphere is challenging because the low density characterizing the atmosphere requires a specific aerodynamic design. In fact, despite Mars's gravity being about 38% of Earth's gravity, density is two orders of magnitude smaller than on Earth, which limits the capability of conventional propellers/wings to provide sufficient thrust/lift. Increasing the speed of aerodynamic surfaces to counteract the low-density effect on aerodynamic forces is constrained by the fact that the speed of sound on Mars is about 75% of the speed of sound on Earth at sea level so that the velocity needed to reach critical Mach numbers is lower on Mars than on Earth. In addition, high speed will also increase drag, which may require additional weight for powerful motors and lead to motor heating issues. The extremely low density makes the force generated by lifting surfaces comparable to their weight, compromising the autonomy, endurance, and maximum payload. The exotic conditions in the Martian atmosphere make optimal aerodynamic design radically different from conventional terrestrial optimality. Therefore, it seems necessary to develop and validate a numerical model able to reproduce ultra-low Reynolds number compressible aerodynamics.

The design of airfoils specifically adapted for Martian atmospheric conditions has been the subject of numerous numerical and experimental studies. The Ultra-low Reynolds number regime, which includes Reynolds numbers between 1,000 and 10,000, is the primary subject of these studies. Notably, [1] carried out one of the first thorough numerical investigations on efficient airfoils and rotors under these circumstances. [2, 3] have presented comprehensive aerodynamic and optimization analyses of airfoils explicitly designed for the Mars environment. For the Mars Science Helicopter (MSH) developed within the Rotor Optimization for the Advancement of Mars eXploration (ROAMX) project [4, 5] selected a sharp leading edge double-edged plate as the airfoil. [6–9] conducted extensive numerical and experimental research on airfoils for their coaxial helicopter design. They employed

Domenic D'Ambrosio contributed equally to this work.

✉ Manuel Carreño Ruiz
manuel.carreno@polito.it

Domenic D'Ambrosio
domenic.dambrosio@polito.it

[1] Department of Mechanical and Aerospace Engineering, Politecnico di Torino, Corso Duca degli Abruzzi 24, 10129 Turin, Italy

Published online: 19 December 2023

XFOIL [10] for the airfoil design, aiming to achieve globally optimal airfoils for various Reynolds numbers and angles of attack. In our work [11–14], we also contributed to the study of airfoils and rotors operating in this regime. We presented the first numerical simulations resulting in different efficient Martian airfoil designs using a coupled Adjoint-based CFD analysis and presented a computationally efficient procedure to generate sharp leading-edge airfoils.

Japanese researchers have made significant contributions to Martian flight research, providing extensive and valuable experimental data gathered from the Martian Wind Tunnel at Tohoku University [15–19]. These findings have served to validate various numerical approaches at these Reynolds numbers, spanning from finite volume Navier–Stokes solvers [9] to high-order DNS (Direct Numerical Simulation) solvers [20]. These works show how including the walls is relevant in order to adequately reproduce the experimental loads on the triangular airfoil wind.

This work extends the preliminary investigation presented by the authors [21] discussing the experimental validation of Navier–Stokes simulations of the triangular airfoil inside a virtual twin of the Martian Wind Tunnel using data from Munday [15]. This work aims to validate and test the Navier-Stokes solver embedded in the commercial CFD code STAR-CCM+ in the high subsonic ultra-low Reynolds number regime. The validation of such an approach on a sharp leading-edge geometry will serve as a starting point to perform the virtual testing of innovative sharp leading-edge geometries that are currently emerging as they pose some benefits due to the formation of laminar separation bubbles that reduce the global viscous drag with a contained pressure drag penalty as shown in [14]. Numerical testing would be very advantageous considering that there are only a handful of facilities in the world that can achieve these Reynolds numbers, and operating them is extremely expensive.

2 Methodology

The simulations presented in this work are fully 3D, as the wing spans the entire test section width, and wall effects may affect separation. Upper walls are also included, with a 1.3° divergence, to account for possible blockage effects caused by the growing boundary layers in the wind tunnel walls. The following sections detail the numerical procedure for reproducing the flow field around the triangular airfoil wing.

2.1 Physical/mathematical model and numerical method

The physical/mathematical model used to simulate the flow field is based on the compressible unsteady Navier Stokes (NS) equations. The implementation is the one offered by the commercial CFD software STAR CCM+, in particular, version 14.06.12. The calculation of inviscid fluxes adopts a second-order reconstruction scheme combined with Roe's scheme, and the evaluation of viscous fluxes uses a second-order approximation. The simulations in the following section employ an implicit second-order time integration scheme, with a time step of 5.10^{-6} s. This time step corresponds with approximately 0.025 convective turnovers. The time step length ensures that the vortex shedding regime is resolved and allows for the convergence of the inner solver, which runs for ten iterations every time step. The total simulation time is 120 convective turnovers, using the last 20 to compute statistics.

2.2 Computational domain and boundary conditions

The adopted computational domain is visible in Fig. 1. We can appreciate how the wind tunnel walls are included. We enforce the freestream, inflow boundary conditions (Mach number, static pressure, and temperature) in the "inflow" section, and we impose the freestream pressure on the

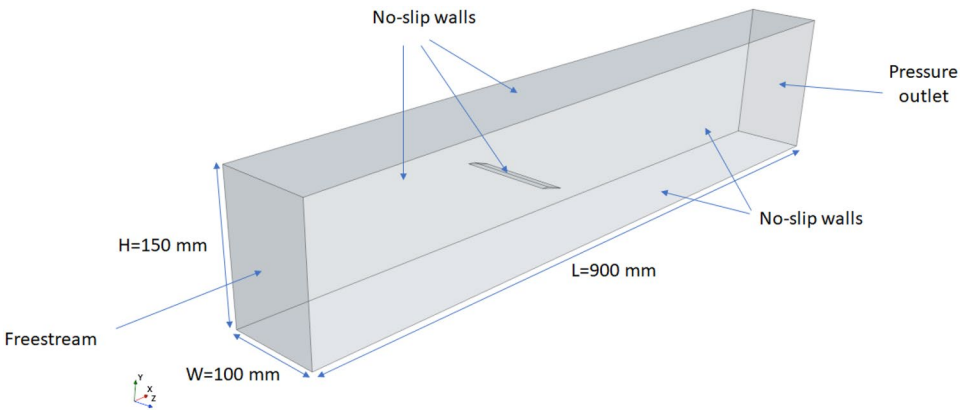

Fig. 1 Fluid domain and boundary conditions

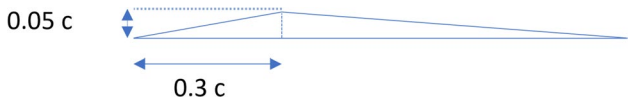

Fig. 2 Airfoil geometry. c = 30 mm

Table 1 Inflow conditions

Mach number	Total pressure (Pa)	Total temperature (K)
0.5	1000	288

"outflow" flat surface normal to the freestream direction. No-slip, adiabatic wall conditions are set on the airfoil surface and wind tunnel walls. As we will show in the next section, the freestream is always aligned with the x-axis, and the airfoil is rotated (and the grid is re-meshed) to account for changes in the angle of attack. The airfoil used to construct the wing is a triangular airfoil with a maximum relative thickness of 5% found at the 30% of the chord as shown in Fig. 2.

Our simulations have been performed at Reynolds number of 3000 and a Mach number of 0.5. However, the actual experimental conditions shown in [15] have been set to model the freestream. These are represented in Table 1.

2.3 Grid generation and refinement analysis

We built the computational meshes using the automated, hexahedral trimmed mesh generation software embedded in STAR-CCM+ in combination with a prism layer mesh in the near-wall region. An adaptive mesh refinement (AMR) strategy has been implemented based on pressure and velocity gradients to reduce the number of cells where they are not needed, for example, near the inflow boundary, where gradients are almost zero. In addition, the AMR approach is quite useful in the low-Reynolds number regime, where the flowfield can change drastically with the angle of attack, moving from fully attached boundary layer situations to the formation of separation bubbles or even massive separations. When the angle of attack exceeds 6 degrees the flow starts to show a vortex shedding. In these cases, we superimpose a volumetric wake refinement to the AMR strategy. This can be seen in Fig. 3, where we can appreciate concentric cylindrical refinement associated with the pressure gradients and the volumetric wake refinement. Figure 4 shows a detail of the grid near the wing. We can appreciate a near-airfoil prism layer and a volumetric refinement with cell size equal to the target airfoil size, which attempts to mesh the airfoil suction and pressure sides with 150 cells. We can also appreciate how a prism layer has been introduced to adequately capture the boundary layers in the wind tunnel walls, potentially causing a flow blockage. This blockage was partially compensated with a 1.3° divergence of the top and bottom walls in the experimental campaign.

The aforementioned grid generation strategy generates grids that range from 10 million cells at zero angle of attack to 20 million cells at 16 degrees. This is caused by the more significant pressure gradients at high lift conditions and by the thicker wake for angles of attack where leading-edge separation is present.

Considering that these simulations are meant to resolve the smallest scales of the flow at which dissipation occurs, typical grid independence analyses used for Reynolds Averaged Navier Stokes (RANS) approaches might not be suitable and would require an intensive computational cost. In this case, to assess the suitability of the grid to discretize our domain, we will compare our grid spacing with the scale at which dissipation occurs, the Kolmogorov length scale, defined as:

$$\eta = (\nu^3/\epsilon)^{0.25} \tag{1}$$

where ν is the kinematic viscosity and ϵ is the energy dissipation rate per unit mass, defined as:

$$\epsilon = 2\nu|S|^2 \tag{2}$$

where S is the strain rate tensor which can be computed from the velocity field as:

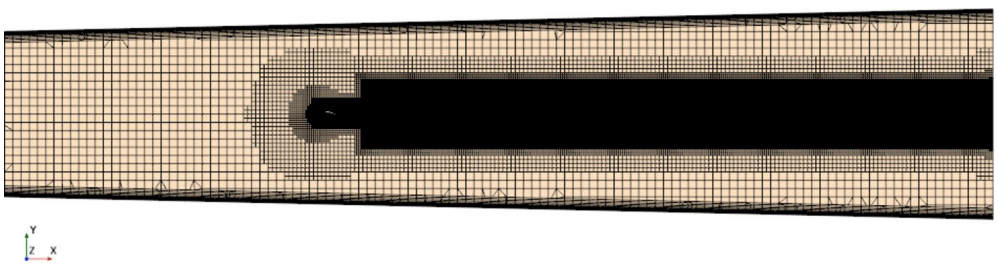

Fig. 3 Computational grid at $\alpha = 14°$

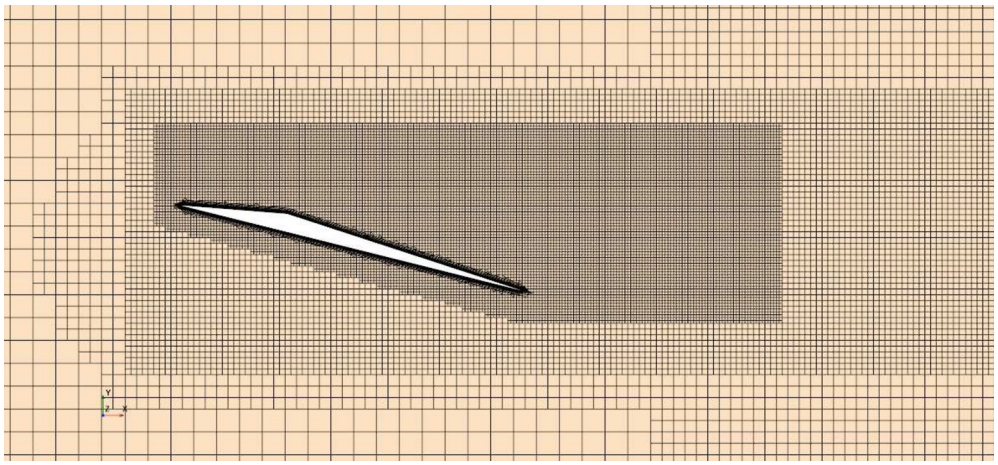

Fig. 4 Computational grid at $\alpha = 14°$. Airfoil Detail

$$S = \frac{1}{2}(\nabla\vec{v} + \nabla\vec{v}^T) \tag{3}$$

Figure 5 shows the ratio between the grid resolution, defined as the cubic root of the cell volume, and Kolmogorov's length scale shown in Eq. 1. It is appreciable how, in the near airfoil region with the finest refinement, the mesh resolution is below 3η. In the wake region, this is relaxed until a value of around 5η. It is worth mentioning that our simulations do not attempt to resolve the wind tunnel boundary layers with a DNS resolution. They just attempt to capture the blockage caused by these and their effect on the average loads over the wing. Despite not being able to call our approach a DNS formally, we are confident that around the airfoil and the near wake region, our grid allows the resolution of the relevant scales that are found in the flow, which will be corroborated by a good agreement with experimental lift and drag coefficients in the following section. Previous work by [20] using a fifth-order flux reconstruction approach by [22] shows, for the same problem at a Mach Number of 0.15, how a grid resolution (divided by the order of the approach) below 2.5η provides adequate DNS resolution. Despite the difference between the approaches employed in order of accuracy (second order vs. fifth order) and methodology (finite volume vs. high order flux reconstruction), both methods should have a comparable equivalent resolution.

To further validate the adequacy of our spatial resolution, we have computed the forces on the wing at a 10-degree angle using a third-order central difference scheme with a 4% upwind blending to stabilize the solver, which is prone to dispersive errors. Increasing the order of accuracy of the spatial discretization effectively enhances the resolution for a given grid, as demonstrated in [20, 23]. Furthermore, central

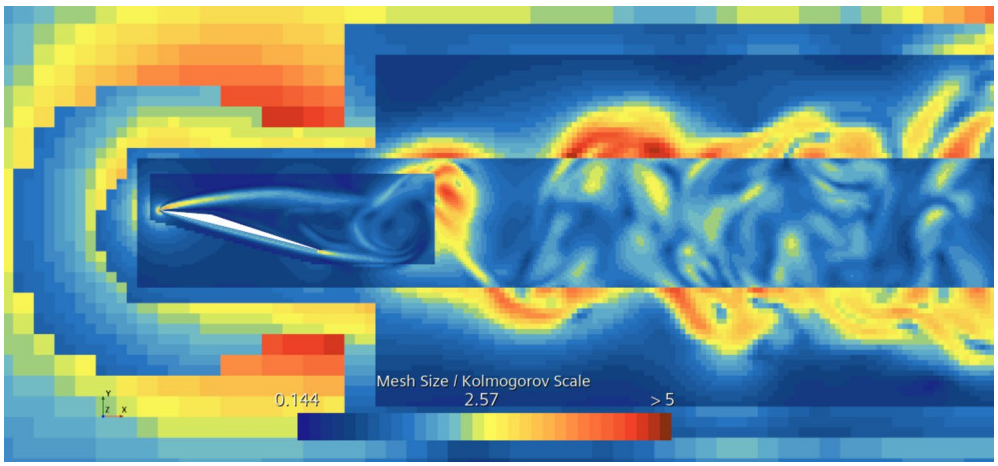

Fig. 5 Numerical simulation of the triangular airfoil wing at AOA = 14°. Ratio between the mesh size and the estimated Kolmogorov length scale in the midplane section

difference schemes exhibit lower dissipative characteristics compared to upwind schemes, which should contribute to better preserving kinetic energy at the smallest scales. Upon comparing the second and third-order accurate solutions, we observed that the differences in the lift and drag coefficients were well below 1%. This observation enhances our confidence in the effectiveness of the computational grid used in this study, indicating that the grid is very suitable for resolving the flow.

3 Results and Comparison

Simulations were run for angles of attack ranging from 0 to 16 degrees in intervals of 2 degrees. The flow conditions present a Reynolds number of 3000 and a Mach number of 0.5.

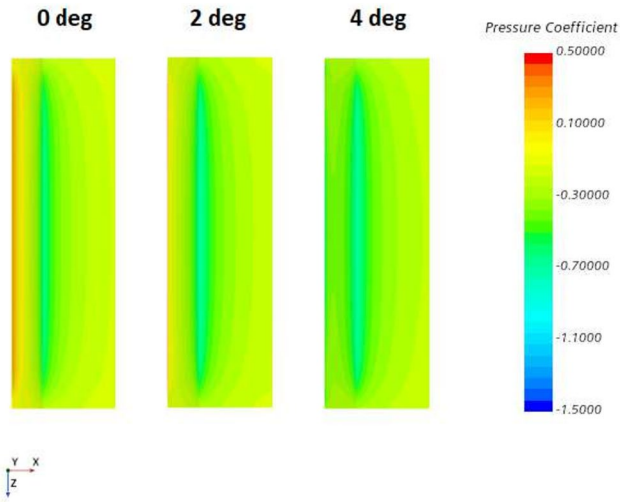

Fig. 6 Pressure coefficient on the suction side

We can distinguish very different flow conditions depending on the angle of attack spanning from steady attached flow to massive leading edge separations. Our simulations have been performed using 64 cores of 2 Intel Xeon Scalable Processors Gold 6130 operating at 2.10 GHz. The average simulation time is around 2500 CPU hours.

Between 0 and 4 degrees, the flow is steady and exhibits a 2-dimensional structure in the central part of the wing, only disturbed by the boundary layers developing in the lateral walls. This is clearly appreciated in Fig. 6 showing a drop of the suction peak near the walls. This will cause a reduction in the global lift coefficient compared to an isolated simulation without walls, showing the importance of including the wind tunnel geometry in the simulation to accurately reproduce the experimental results. Figures 7 and 8 show how for angles of attack 0 and 2 degrees, the flow presents an attached flow with very thick boundary layers. At 4 degrees, the boundary layer separates before the trailing edge creating a steady spanwise vortex towards the trailing edge as shown in Fig. 9.

At the angle of attack of 6 degrees, the flow separates at the apex of the airfoil, as shown in Fig. 10. In this case, the flow is unsteady, showing a quasi-two-dimensional Kàrman vortex street only deformed by the wind tunnel walls. Figure 17 shows how these vortices are fairly stable and are not broken down into smaller structures. The visualization of the vortices is accomplished by plotting iso-surfaces of the Lambda-2 criterion defined as the second eigenvalue of the matrix obtained by adding the squares of the symmetric and anti-symmetric components of the velocity gradient tensor. For an angle of attack of 8 degrees (Fig. 11), we can appreciate a separation of the boundary layer at the apex shedding vortices into the wake, but in this case, these spanwise vortices start to become unstable and present secondary braids as shown in Fig. 18.

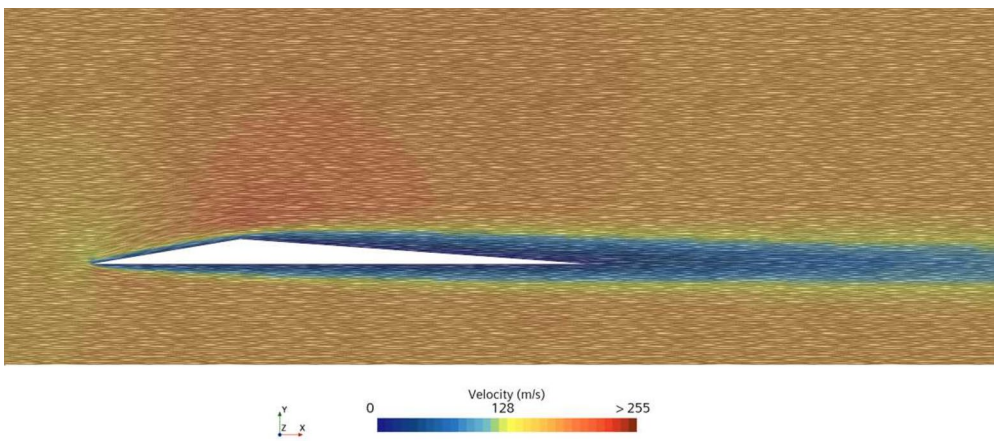

Fig. 7 Numerical simulation of the triangular airfoil wing at AOA = 0°. Instantaneous velocity streamlines projected into the mid-span section of the wind tunnel

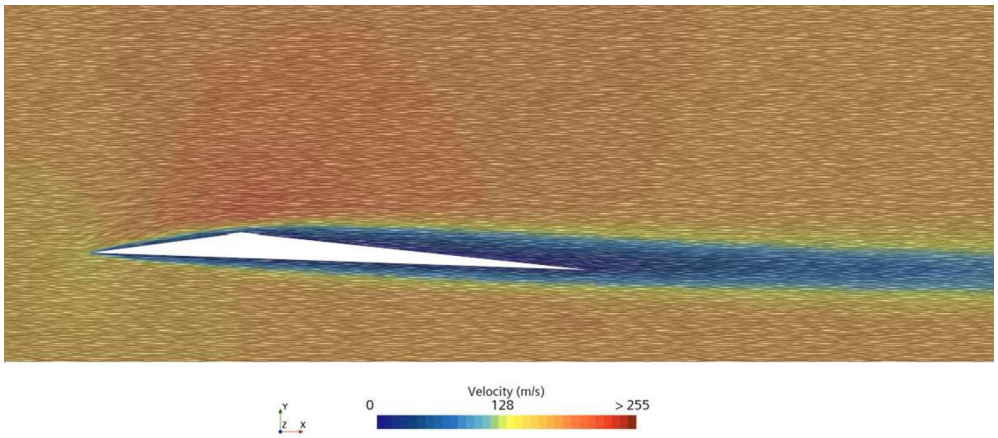

Fig. 8 Numerical simulation of the triangular airfoil wing at AOA = 2°. Instantaneous velocity streamlines projected into the mid-span section of the wind tunnel

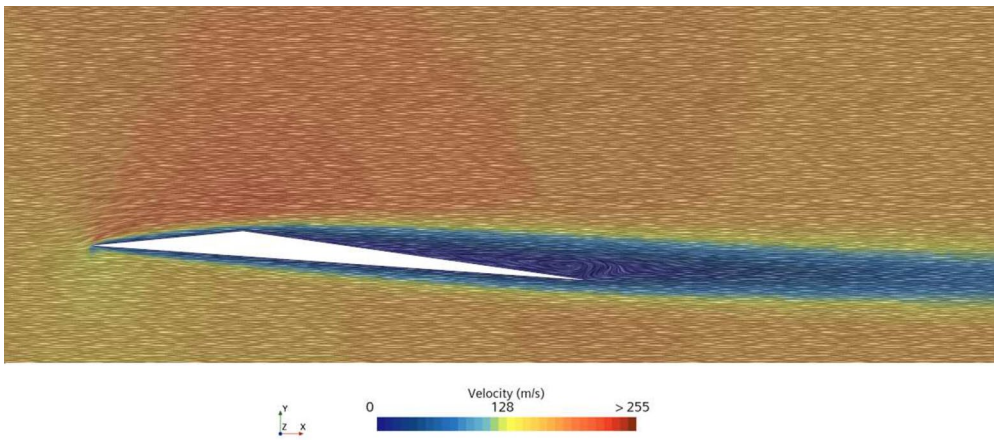

Fig. 9 Numerical simulation of the triangular airfoil wing at AOA = 4°. Instantaneous velocity streamlines projected into the mid-span section of the wind tunnel

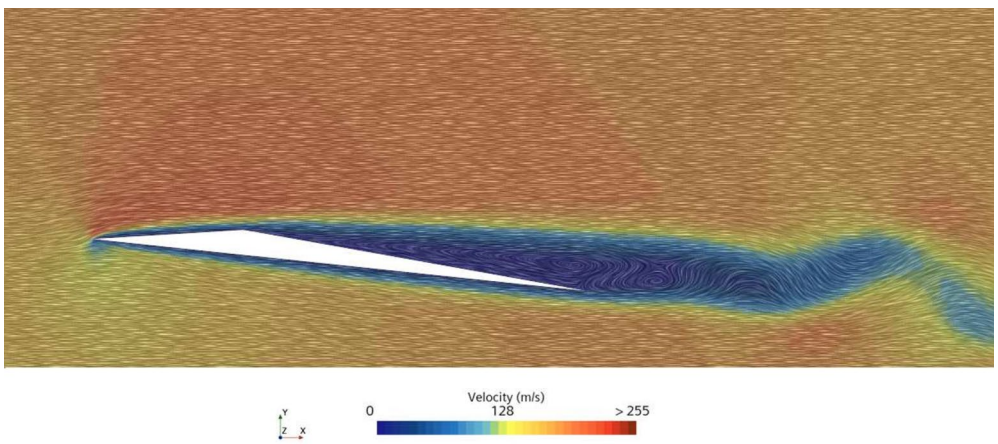

Fig. 10 Numerical simulation of the triangular airfoil wing at AOA = 6°. Instantaneous velocity streamlines projected into the mid-span section of the wind tunnel

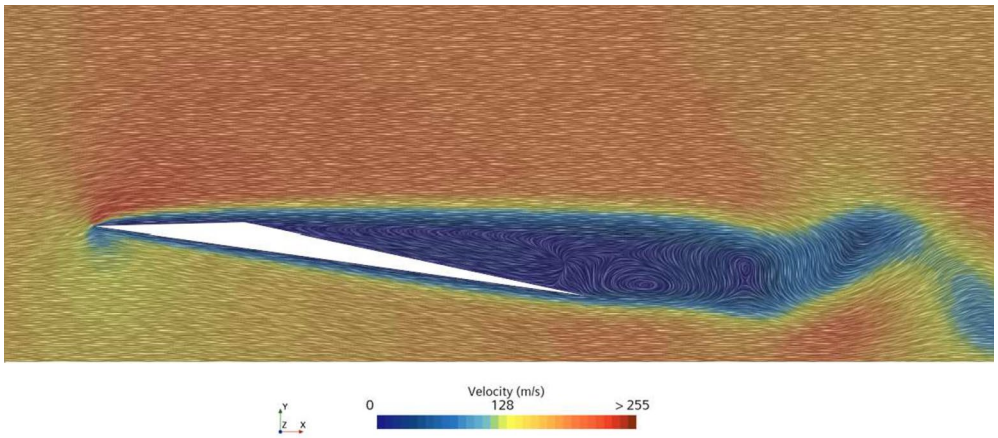

Fig. 11 Numerical simulation of the triangular airfoil wing at AOA = 8°. Instantaneous velocity streamlines projected into the mid-span section of the wind tunnel

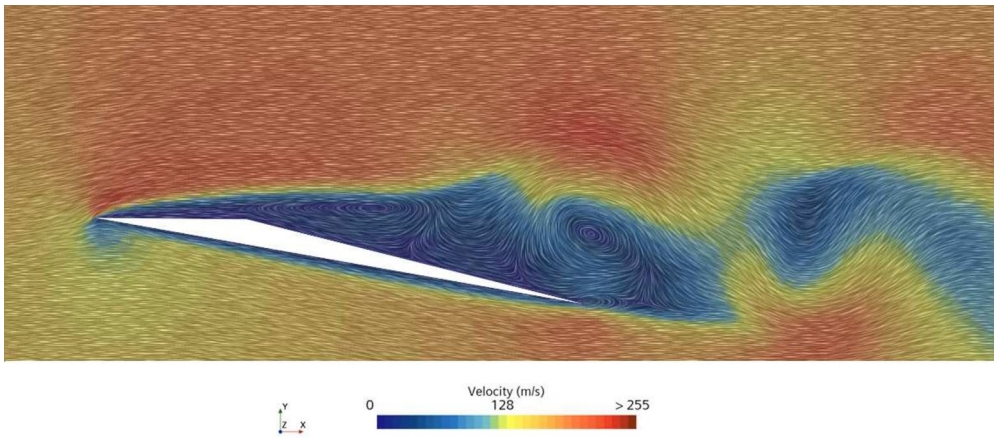

Fig. 12 Numerical simulation of the triangular airfoil wing at AOA = 10°. Instantaneous velocity streamlines projected into the mid-span section of the wind tunnel

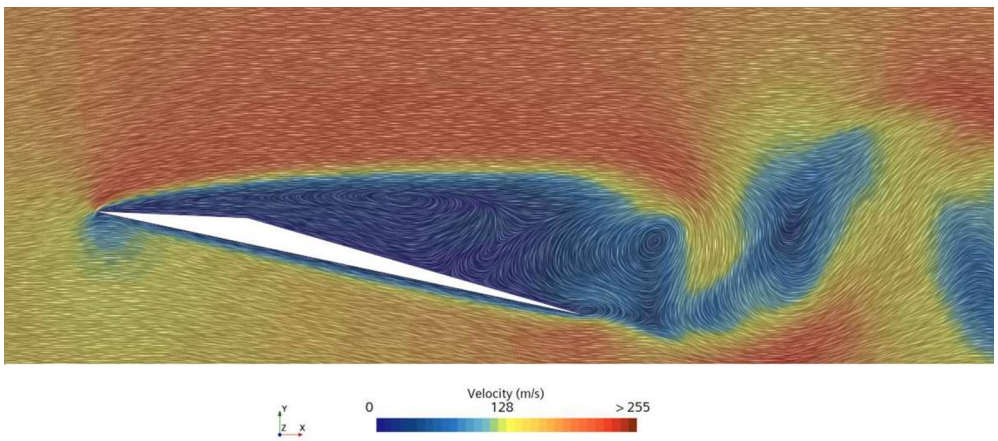

Fig. 13 Numerical simulation of the triangular airfoil wing at AOA = 12°. Instantaneous velocity streamlines projected into the mid-span section of the wind tunnel

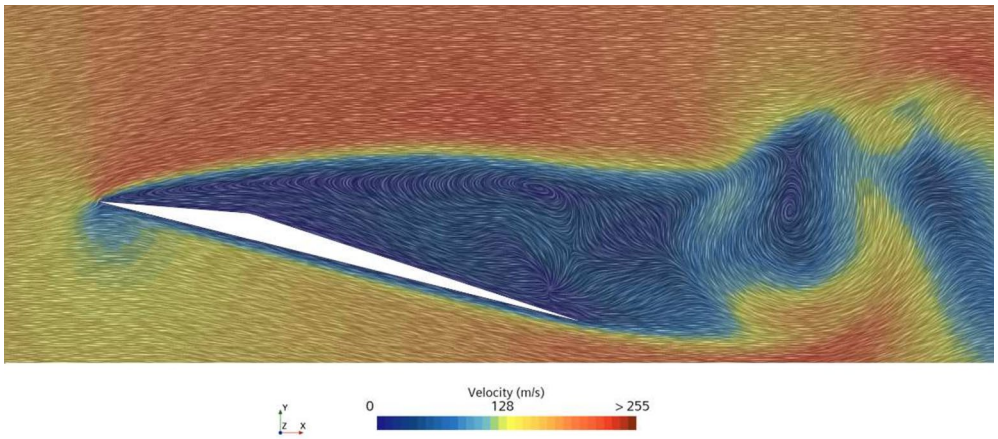

Fig. 14 Numerical simulation of the triangular airfoil wing at AOA = 14°. Instantaneous velocity streamlines projected into the mid-span section of the wind tunnel

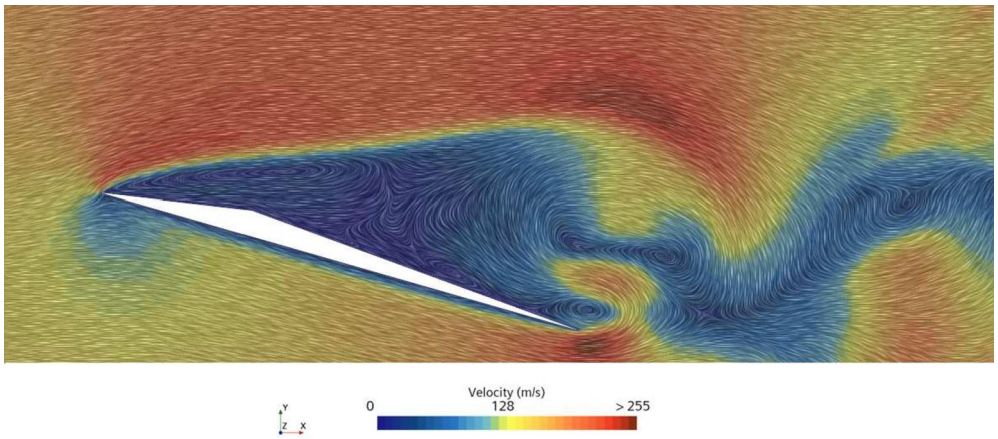

Fig. 15 Numerical simulation of the triangular airfoil wing at AOA = 16°. Instantaneous velocity streamlines projected into the mid-span section of the wind tunnel

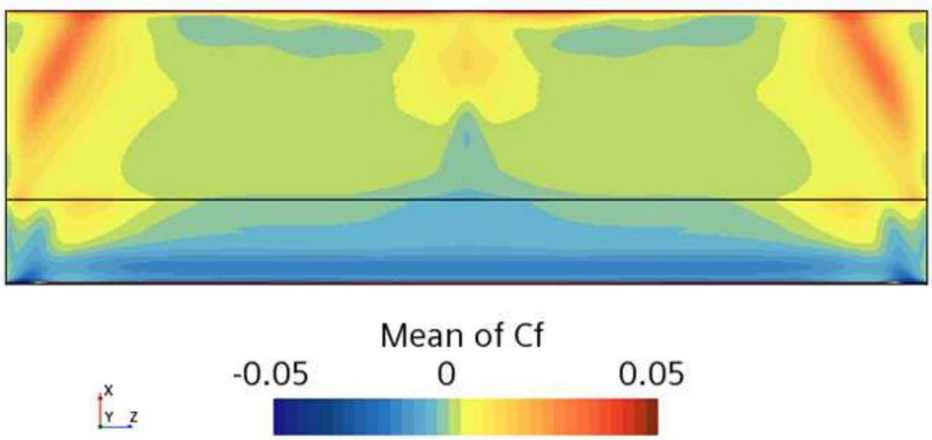

Fig. 16 Mean chordwise friction coefficient on the suction side. AOA = 10°

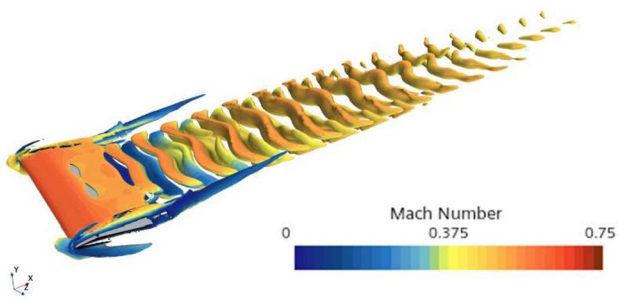

Fig. 17 Numerical simulation of the triangular airfoil wing at AOA = 6°. Lambda-2 iso-surfaces colored with Mach number contours

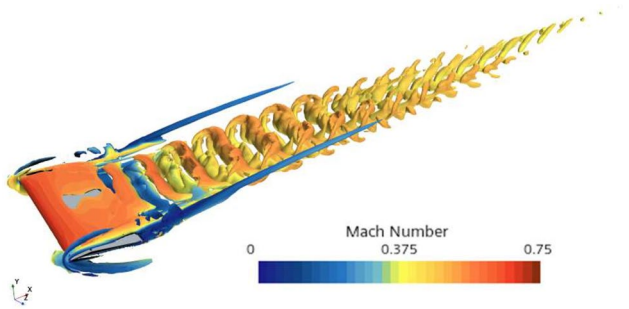

Fig. 18 Numerical simulation of the triangular airfoil wing at AOA = 8°. Lambda-2 iso-surfaces colored with Mach number contours

When the angle of attack reaches 10 degrees, Fig. 12, the boundary layer geometrically separates at the leading edge, but the fact that the front plane of the suction side is approximately aligned with the flow direction helps the boundary layer to reattach, avoiding a massive leading edge separation. Figure 16 shows how, after negative values of the chordwise friction coefficient near the leading edge, these increase, achieving values of approximately zero. In the same figure, we can also appreciate the three-dimensionality of the flow over the wing after the apex. In fact, when the apex is reached, the already thick boundary layer rolls up and breaks down into smaller structures above the suction side of the airfoil, creating a fully three-dimensional wake as shown in Fig. 19.

As we increase the angle of attack beyond ten degrees, separation occurs directly at the leading edge, as shown in Figs. 13, 14, 15, causing a massive separation Figs. (16, 17, 18, 19). The instabilities are intensified, creating smaller structures in the wake, as shown in Figs. 20, 21, 22. Furthermore, the wakes become progressively thicker as the angle of attack increases.

Regarding the overall flow inside the wind tunnel, Fig. 23 shows the instantaneous Mach number field on the wind tunnel's mid-span section for an angle of attack of 14 degrees. It is clearly appreciated how the separation occurs in the leading edge and shows massive separation with a three-dimensional and very thick wake. We can appreciate how boundary layers grow significantly and how the 1.3° divergence helps to compensate for the blockage effect.

The different flow regimes recovered with this approach align with those computed by [15] performing a DNS without the wind tunnel walls. However, the forces computed by [15] do not show a good agreement with their experimental measurements. Figures 24 and 25 present our computed lift and drag coefficients compared to the experimental values measured by [15]. We can appreciate a satisfactory agreement for low and moderate angles of attacks. Slight differences are found for the largest angles of attack where the flow becomes completely three-dimensional. In these cases, the error could possibly be related to the temporal and spatial discretizations that may need refining to capture higher frequency structures outside the finely refined region. The lift coefficient shows a non-linear pattern increasing its slope significantly after 10 degrees when the boundary layer separates at the leading edge. This increase in lift can be justified by the low-pressure vortex cores traveling closely above the airfoil's suction side.

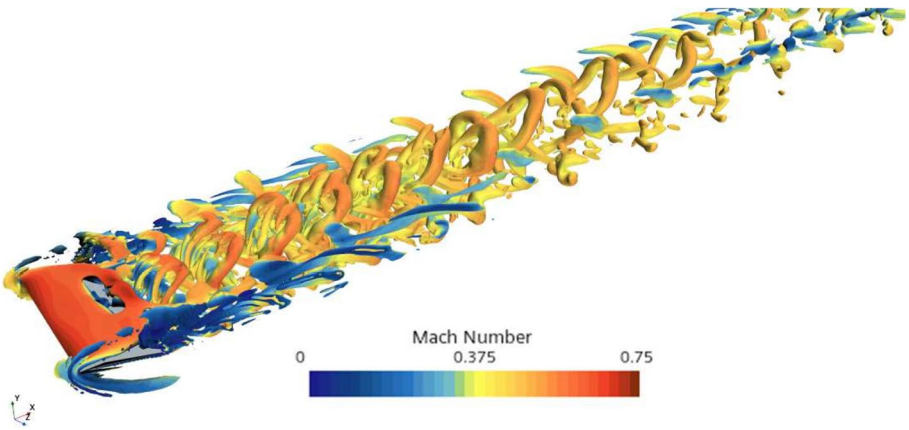

Fig. 19 Numerical simulation of the triangular airfoil wing at AOA = 10°. Lambda-2 iso-surfaces colored with Mach number contours

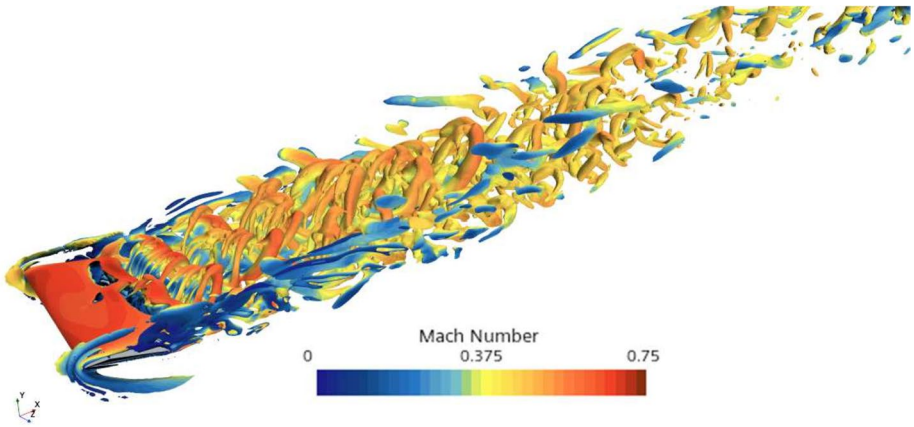

Fig. 20 Numerical simulation of the triangular airfoil wing at AOA = 12°. Lambda-2 iso-surfaces colored with Mach number contours

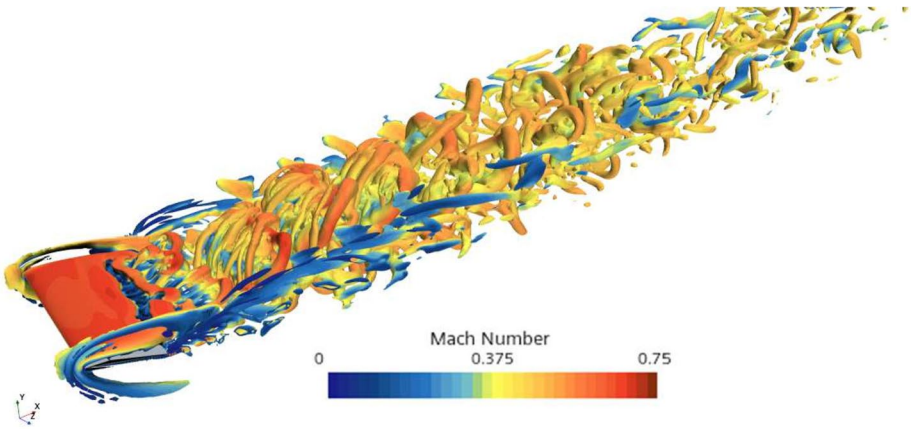

Fig. 21 Numerical simulation of the triangular airfoil wing at AOA = 14°. Lambda-2 iso-surfaces colored with Mach number contours

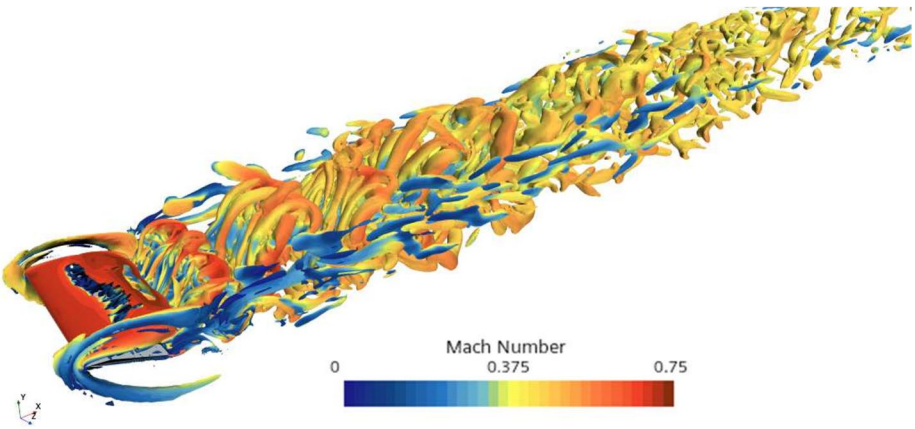

Fig. 22 Numerical simulation of the triangular airfoil wing at AOA = 16°. Lambda-2 iso-surfaces colored with Mach number contours

These results also align with [9], which used STAR-CCM+ and elsa, ONERA's in-house CFD code, to solve the same problem but only at 10 degrees. One can also appreciate qualitative similarities with results presented by [20], who performed a DNS on this airfoil using PyFR despite the different Mach number of 0.15. Thus, this work extends the validation performed by different authors for a range of angles of attack and a high subsonic Mach number. The aforementioned studies also show qualitatively similar behaviors comparing 2D simulations and periodic 3D simulations for low and moderate angles of attack. This fact provides confidence in using 2D compressible Navier-Stokes

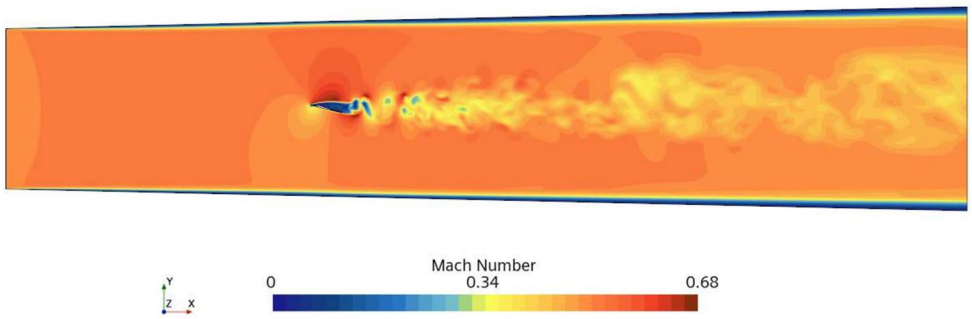

Fig. 23 Numerical simulation of the triangular airfoil wing at AOA = 14°. Instantaneous Mach number in the mid-span section of the wind tunnel

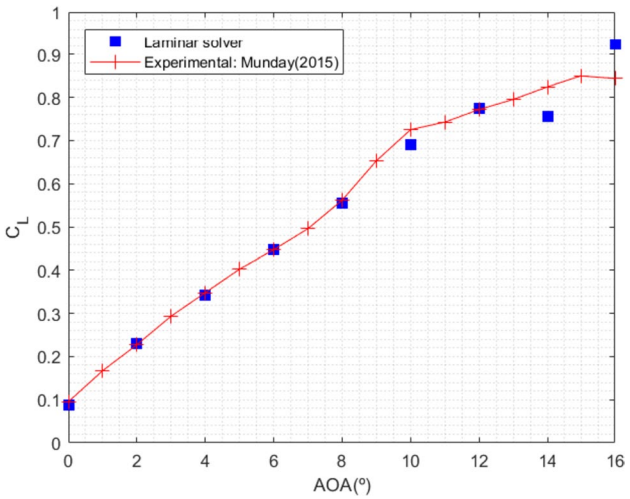

Fig. 24 Comparison between experimental and numerical airfoil lift coefficient for Reynolds number of 3000 and Mach number of 0.5

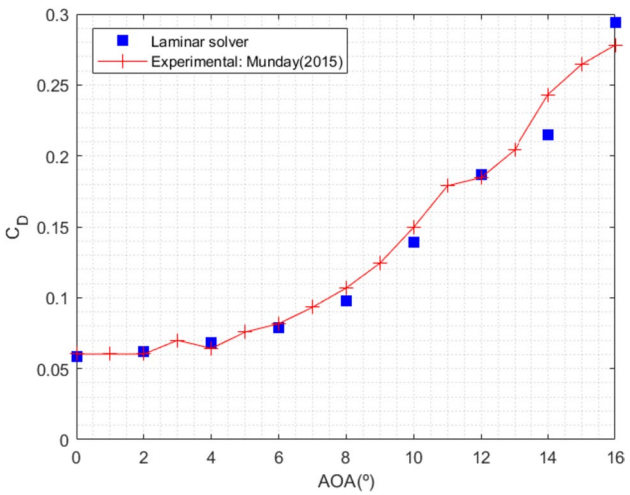

Fig. 25 Comparison between experimental and numerical airfoil drag coefficient for Reynolds number of 3000 and Mach number of 0.5

simulations for optimization and design purposes in this regime for low and moderate angles of attack.

4 Conclusions

A validation exercise of the Navier–Stokes solver embedded in STAR-CCM+ was successfully performed replicating an experiment done at the Martian Wind Tunnel (MWT) at Tohoku University (Japan), where a triangular airfoil wing was tested at Reynolds numbers as low as 3000 and a Mach number of 0.5.

The flow remains steady for angles of attack below 6 degrees. A slight unsteadiness is noticed starting at AOA = 6°, which becomes stronger as the angle of attack increases. At 6 degrees, a quasi-2D vortex shedding is obtained. At an angle of attack of ten degrees, these vortices become unstable and break down into three-dimensional structures. The difference in the flow characteristics is related to the flow separation position. When the flow separates at the apex, the flow remains quasi-2D over the surface of the airfoil. Conversely, when separation occurs at the leading edge, the flow will likely become three-dimensional.

The ability of our numerical setup to capture flow characteristics of a sharp leading edge airfoil is very interesting as recently, the design of these geometries is becoming popular due to their ability to generate optimal separation bubbles on the suction side of airfoils. Sharp leading edges can be seen as a passive flow control mechanism that triggers a laminar separation bubble that, for adequately designed airfoils, generates a reduced shear drag coefficient with a small pressure drag penalization, enhancing the overall airfoil performance.

Overall the good agreement obtained shows how well-resolved Navier–Stokes evaluations using a low-order (Second) finite volume solver can capture ultra-low Reynolds number aerodynamics even for 3-Dimensional unsteady flows, including the interaction with the wind tunnel boundary layers. It is worth noting that for higher Reynolds numbers, the flow will likely break down into smaller structures that would render the solution with a second-order method very demanding. Therefore, the use of a higher-order solver could be advantageous in these cases.

It is also worth mentioning that the present virtual testing methodology shows the ability of numerical models to

reproduce experiments on very complex flow conditions, which are extremely difficult to replicate in a controlled environment. The fact of using an unstructured grid methodology generalizes the approach to potentially much more complex geometries and operating conditions such as those found in rotors. Furthermore, creating a virtual testing environment able to reproduce Martian conditions opens the door to multiphysics simulations of UAS maneuvers with accurate gravitational acceleration, which is impossible to replicate experimentally on planet Earth.

Data availability The datasets generated during and/or analysed during the current study are available from the corresponding author on reasonable request.

Declarations

Conflict of interest The authors declare no conflict of interest.

References

1. Kunz, P.J.: Aerodynamics and design for ultra-low Reynolds number flight. PhD thesis, Standford University (2003)
2. Koning, W.J., Johnson, W., Allan, B.G.: Generation of mars helicopter rotor model for comprehensive analyses. AHS Aeromech. Des. Transf. Vert. Flight (2018)
3. Koning, W.J., Romander, E.A., Johnson, W.: Optimization of low Reynolds number airfoils for Martian rotor applications using an evolutionary algorithm. In: AIAA SciTech 2020 Forum, Orlando, FL (2020)
4. Cummings, H., et al.: Overview and introduction of the rotor optimization for the advancement of mars exploration (ROAMX) project. In: Aeromechanics for Advanced Vertical Flight Technical Meeting, Transformative Vertical Flight 2022 (2022)
5. Johnson, W., et al.: Mars science helicopter conceptual design. NASA/TM-2020-220485. https://rotorcraft.arc.nasa.gov/Publications/files/MSH_WJohnson_TM2020rev.pdf (2020)
6. Bézard, H., Désert, T., Moschetta, J.-M., Jardin, T.: Aerodynamic design of a Martian micro air vehicle. In: EUCASS 2019, MADRID, Spain. https://hal.archives-ouvertes.fr/hal-02397054 (2019)
7. Bézard, H., Désert, T., Jardin, T., Moschetta, J.-M.: Numerical and experimental aerodynamic investigation of a micro-UAV for flying on Mars. In: 76th Annual Forum & Technology Display, Virginia Beach, VA. hal-02901622. https://hal.science/hal-02901622/document (2020)
8. Désert, T., Moschetta, J.-M., Bézard, H.: Numerical and experimental investigation of an airfoil design for a Martian micro rotorcraft. Int. J. Micro Air Veh. **10**(3), 262–272 (2018). https://doi.org/10.1177/1756829318794171
9. Désert, T., Jardin, T., Bézard, H., Moschetta, J.-M.: Numerical predictions of low Reynolds number compressible aerodynamics. Aerosp. Sci. Technol. **92**, 211–223 (2019). https://doi.org/10.1016/j.ast.2019.05.064
10. Drela, M.: Xfoil: An analysis and design system for low Reynolds number airfoils. In: Low Reynolds Number Aerodynamics: Proceedings of the Conference Notre Dame, Indiana, USA, 5–7 June 1989, pp. 1–12. Springer (1989)
11. Carreño Ruiz, M., D'Ambrosio, D.: Aerodynamic Optimization of Quadrotor Blades Operating in the Martian Atmosphere. In: AIAA SciTech 2022 Forum, San Diego. (2022)
12. Carreño Ruiz, M., D'Ambrosio, D.: Aerodynamic optimization and analysis of quadrotor blades operating in the Martian atmosphere. Aerosp. Sci. Technol. **132**, 108047 (2023). https://doi.org/10.1016/j.ast.2022.108047
13. Carreño Ruiz, M., D'Ambrosio, D.: Hybrid fidelity optimization of efficient airfoils and rotors in ultra-low reynolds numbers conditions. In: AIAA SciTech 2023 Forum, National Harbor, MD (2023). https://doi.org/10.2514/6.2023-0652
14. Carreño Ruiz, M., Renzulli, L., D'Ambrosio, D.: Airfoil optimization for rotors operating in the ultra-low Reynolds number regime. Phys. Fluids **35**(10), 103603 (2023). https://doi.org/10.1063/5.0166170
15. Munday, P.M., Taira, K., Suwa, T., Numata, D., Asai, K.: Nonlinear lift on a triangular airfoil in low-Reynolds-number compressible flow. J. Aircraft **52**(3), 924–931 (2015). https://doi.org/10.2514/1.C032983
16. Anyoji, M., Nonomura, T., Aono, H., Oyama, A., Fujii, K., Nagai, H., Asai, K.: Computational and experimental analysis of a high-performance airfoil under low-Reynolds-number flow condition. J. Aircraft **51**(6), 1864–1872 (2014). https://doi.org/10.2514/1.C032553
17. Suwa, T., Nose, K., Numata, D., Nagai, H., Asai, K.: Compressibility effects on airfoil aerodynamics at low Reynolds number. AIAA, New Orleans, LA (2012). https://doi.org/10.2514/6.2012-3029. AIAA-2012-3029
18. Anyoji, M., Nagai, H., Asai, K.: Development of low density wind tunnel to simulate atmospheric flight on Mars. In: 47th AIAA Aerospace Sciences Meeting Including The New Horizons Forum and Aerospace Exposition, Orlando, FL (2009). https://doi.org/10.2514/6.2009-1517. AIAA-2009-1517
19. Anyoji, M., Nose, K., Ida, S., Numata, D., Nagai, H., Asai, K.: Low Reynolds number airfoil testing in a Mars wind tunnel. AIAA, Chicago, IL (2010). https://doi.org/10.2514/6.2010-4627. AIAA 2010-4627
20. Caros, L., Buxton, O., Shigeta, T., Nagata, T., Nonomura, T., Asai, K., Vincent, P.: Direct numerical simulation of flow over a triangular airfoil under Martian conditions. AIAA J. **60**(7), 3961–3972 (2022). https://doi.org/10.2514/1.J061454
21. Carreño Ruiz, M., D'Ambrosio, D.: Validation and application of aerodynamic simulations in the Martian atmosphere. In: 26th Conference of the Italian Association of Aeronautics and Astronautics-AIDAA 2021 (2021)
22. Huynh, H.T.: A flux reconstruction approach to high-order schemes including discontinuous Galerkin methods. In: 18th AIAA Computational Fluid Dynamics Conference, Miami, FL (2007)
23. Ricci, F., Silva, P.A., Tsoutsanis, P., Antoniadis, A.F.: Hovering rotor solutions by high-order methods on unstructured grids. Aerosp. Sci. Technol. **97**, 105648 (2020)